Simultaneous inversion of shear wave splitting observations from seismic arrays

T. Ryberg, G. Rümpker,[1] C. Haberland, D. Stromeyer, and M. Weber
GeoForschungsZentrum Potsdam, Potsdam, Germany

Received 7 July 2004; revised 1 November 2004; accepted 10 December 2004; published 4 March 2005.

[1] Seismic waveforms recorded at high-density receiver arrays facilitate the application of new inversion techniques, which take advantage of the coherent nature of the observations. We use measurements of shear wave splitting parameters from observed *SKS* waveforms along a dense receiver profile and compare them with splitting parameters obtained from numerical waveform modeling through anisotropic Earth models. We use two different iterative approaches for the inversion of the observed splitting parameters (1) a local optimization technique (the downhill simplex method) and (2) a global genetic algorithm search. In our forward modeling, we calculate *SKS* waveforms by a finite difference (FD) method solving the anisotropic wave equation, instead of deriving individual anisotropic models for each station and combining them into one model. By the comparison of FD modeling and observations we avoid a direct interpretation of the splitting parameters in terms of medium properties. We apply these techniques to the analysis of *SKS* phases recorded along a 100-km profile located at the Dead Sea transform fault. The measured splitting parameters show gradual short-scale variations along the profile which depend on frequency. Lateral and vertical variations of anisotropy are accounted for by two-dimensional block structures. For the simplex method the complexity of the models (the number of anisotropic blocks) is increased gradually, whereas the number of anisotropic blocks is kept fixed for the genetic algorithm search. The anisotropic structures of the best fitting models derived from the two inversion approaches agree well. The results support earlier interpretations of the observations in terms of a narrow, approximately 20 km wide, vertical decoupling zone in the mantle that accommodates the transform motion between the African and Arabian plates.

Citation: Ryberg, T., G. Rümpker, C. Haberland, D. Stromeyer, and M. Weber (2005), Simultaneous inversion of shear wave splitting observations from seismic arrays, *J. Geophys. Res.*, *110*, B03301, doi:10.1029/2004JB003303.

1. Introduction

[2] In recent years, there have been numerous observations of complex inhomogeneous elastic anisotropy in the Earth's crust and mantle. Studies of *SKS* splitting from dense seismic networks show pronounced variations of splitting parameters over distances of less than 50 km in regions of the San Andreas Fault [*Hartog and Schwartz*, 2000; *Polet and Kanamori*, 2002], the Tibetan Plateau [*Huang et al.*, 2000], the Nazca subduction zone [*Russo and Silver*, 1994; *Polet et al.*, 2000; *Bock et al.*, 1998], and the Eifel region [*Walker et al.*, 2005]. Furthermore, observed changes of splitting parameters as function of back azimuth and frequency cannot be explained on the basis of homogeneous anisotropy [*Silver and Savage*, 1994; *Marson-Pidgeon and Savage*, 1997; *Brechner et al.*, 1998; *Hartog and Schwartz*, 2001] and require more complex anisotropic structures. Observations of such *SKS* splitting variations provide important constraints for models of mantle deformation and have been interpreted in terms of three-dimensional mantle flow models [*Russo and Silver*, 1994; *Fouch et al.*, 2000]. In addition, there is evidence from numerical modeling of the lattice-preferred orientation of olivine crystals near mid-ocean ridges [*Blackman et al.*, 1996] and subduction zones [*Fischer et al.*, 2000; *Hall et al.*, 2000] for the development of inhomogeneous anisotropy.

[3] Conventionally, *SKS* splitting observations are analyzed independently for each seismic station, and the joint analysis of the results is part of the interpretation process. However, waveforms from high-density one- and two-dimensional seismic arrays facilitate the application of new data processing and inversion techniques, which exploit the coherent nature of the recordings at neighboring stations. In the approach described here, the simultaneous inversion of the observations is performed for a station spacing that is significantly smaller than the Fresnel zone width of the phases to be analyzed. For example, *SKS* phases with a period of about 4 s have a Fresnel zone of $\sim$50 km for anisotropic structures at 50 km depth [*Rümpker and Ryberg*, 2000]. Such sub-Fresnel zone station spacing

[1] Now at Fachbereich Geowissenschaften/Geographie, J. W. Goethe-Universität Frankfurt, Frankfurt am Main, Germany.

0148-0227/05/2004JB003303$09.00

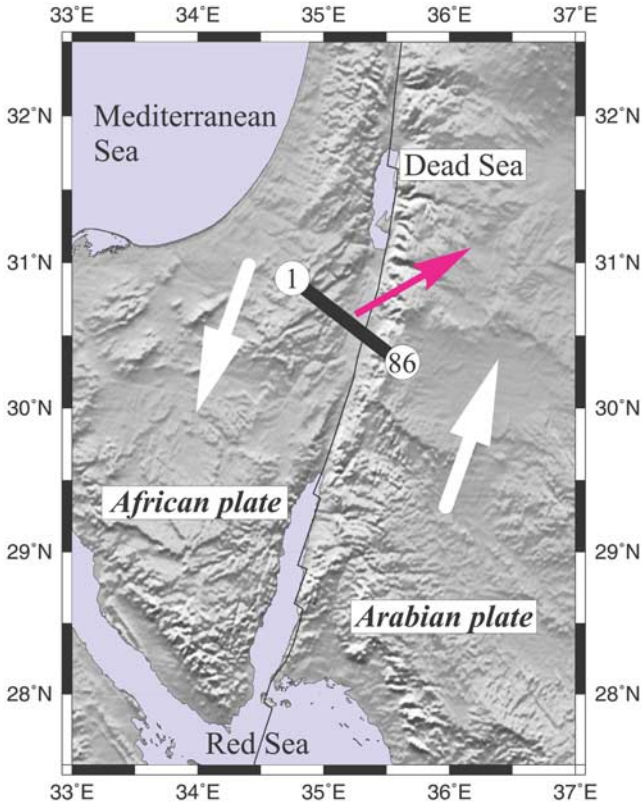

Figure 1. Location map of the profile across the Dead Sea transform fault between the Dead Sea and the Red Sea. The average station spacing along the profile is 1.2 km; the numbers refer to stations at the end points of the profile. Arrows indicate the relative plate motions (in white) and the back azimuth (in red) of the event used in the analysis. Event origin time is 28 March 2000, 1100:22.5 UT; hypocenter coordinates are 22.338°N, 143.730°E; depth is 127 km; M_w = 7.6.

does not imply that the waveform effects at neighboring stations are the same. The modeling of *SKS* splitting effects for media with sharp anisotropy contrasts shows that waveforms and splitting parameters exhibit rather smooth variations along profiles crossing an inhomogeneous region [*Alsina and Snieder*, 1995; *Rümpker and Ryberg*, 2000]. The observation of the associated waveform coherency not only provides insights into the small-scale structure of anisotropy beneath the array but also lends additional confidence to the accuracy of the measurements. Also, the associated waveform diffraction effects can provide further constraints for the modeling. Accounting for these effects requires the application of appropriate forward modeling tools. We therefore use a finite difference formulation of the anisotropic wave equation for inhomogeneous media to derive suitable Earth models.

[4] The methodology presented here has been developed to analyze *SKS* waveforms from a dense one-dimensional array across the Dead Sea transform fault [*Rümpker et al.*, 2003]. There we used a simplex inversion algorithm to derive suitable models of the anisotropic structure in the crust and mantle beneath the fault. Here, the inversion process is performed more systematically and tested for a much larger number of models. In addition to this, we employ also a more global parameter search based on a genetic algorithm search. The resulting models that explain the observations are analyzed in terms of cluster analysis. Although our data analysis is limited to a single seismic event, the short-scale and frequency-dependent variations of splitting parameters are exploited to resolve the depth-dependent anisotropic structure along the profile. The characteristic features of the models derived on the basis of the different methods are very similar, which supports the earlier interpretation of our results in terms of a narrow highly anisotropic boundary zone between the African and Arabian plates.

2. Waveform Data and Shear Wave Splitting Analysis

[5] The *SKS* waveforms used in this study were recorded from a single event at 86 stations along a 100-km profile across the Dead Sea transform fault (Figure 1; see *Rümpker et al.* [2003] and *DESERT Group* [2004] for details). The horizontal components along the profile exhibit smoothly varying amplitudes over a relatively short length scale (Figure 2). A nonvanishing transverse component of the *SKS* phase is usually considered to be indicative of shear wave splitting due to anisotropic structures within the mantle and crust beneath the receiver. After a conventional spectral analysis of the rotated (radial and transverse) components, we calculated the transverse/radial amplitude ratio as a function of frequency (Figure 3). This allows the identification of period ranges that exhibit effects of shear wave splitting and can therefore be analyzed in terms of splitting parameters. The initial reason for taking this

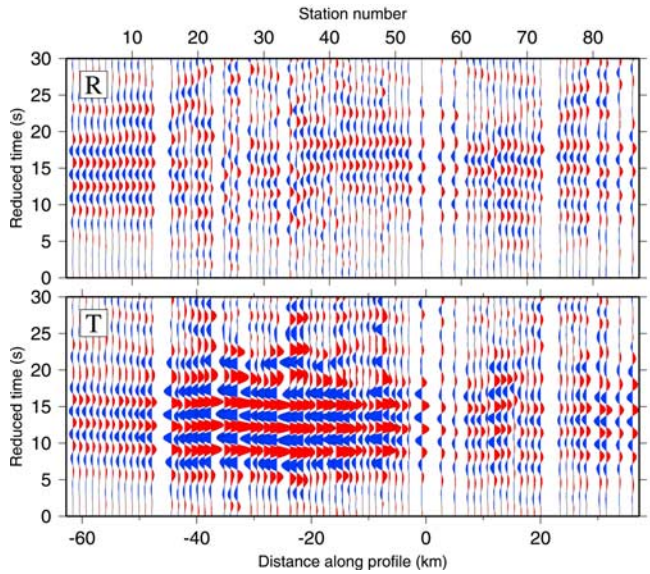

Figure 2. Radial (R) and transverse (T) components of *SKS* waveforms used in this study. The amplitude scale is identical for all traces. An explanation of the large transverse amplitudes is given in Appendix A. The traces are shown with respect to the distance along the profile, where the origin corresponds to the surface location of the Dead Sea transform fault. A band pass filter between 2 and 5 s has been applied to the seismograms.

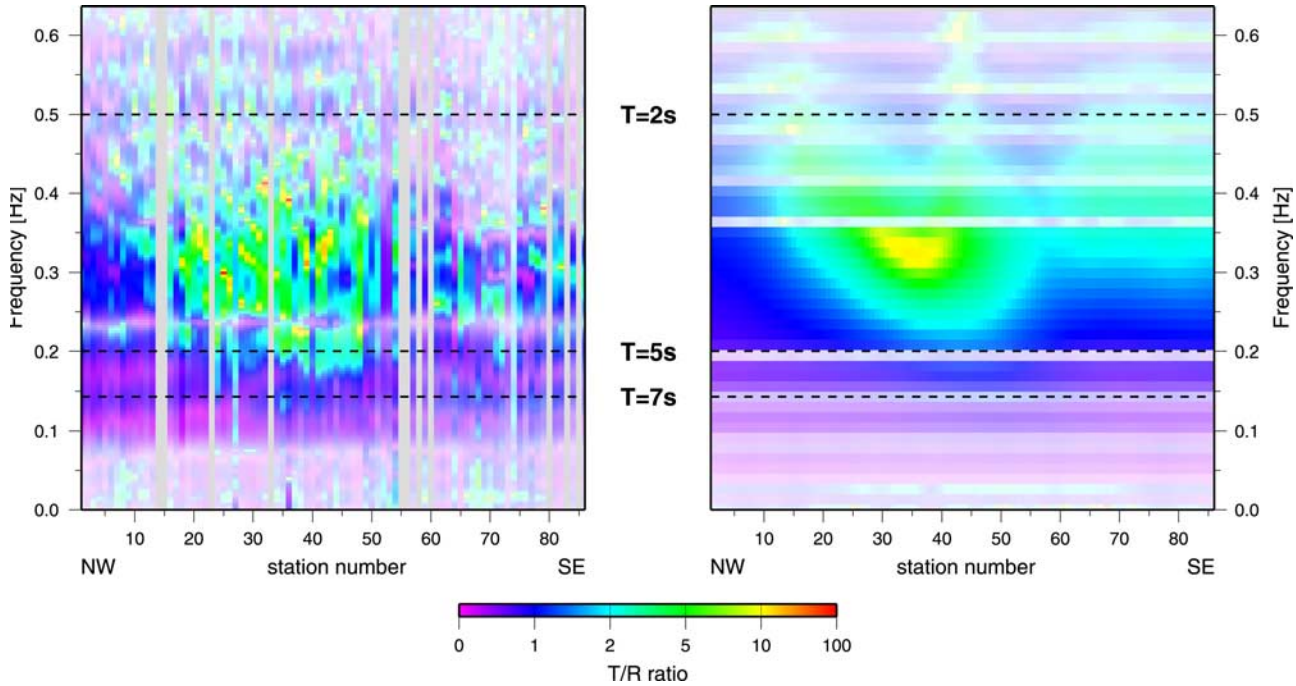

Figure 3. Color-coded frequency-dependent amplitude ratios of the transverse and radial component (T/R) (left) for the studied earthquake and (right) for the synthetic seismograms corresponding final model (discussed later). Saturated colors indicate strong energies on horizontal components, thus indicating regions with relatively high signal-to-noise ratios of the transverse and radial components. The color saturation is proportional to $\sqrt{R^2 + T^2}$, where R and T are the spectral values of the transverse and radial components. Note that the T/R ratio is unusually high for higher frequencies in a region NW of the Dead Sea transform fault, which is located at station 54. Black dashed lines show the two frequency bands for which splitting parameters are analyzed. Vertical gray lines (left) are missing or poor traces. Gray horizontal lines (right) are related to the source time function.

approach was that short-period (1 Hz) sensors were used in the experiment and that the dominant period of *SKS* phases is usually much longer (about 8 s). Our analysis shows that the largest transverse components along the profile are found between stations 18 and 50 at periods between 2 and 5 s (see Appendix A for a more detailed explanation of the dominant transverse amplitudes). Significant transverse amplitudes are also found at longer periods between 5 and 10 s. However, the lateral variations along the profile are strongly reduced at longer periods. In view of these observations, we decided to perform the splitting analysis for two distinct period ranges, with a short-period band between 2 and 5 s and a long-period band between 5 and 7 s. In the process of the analysis an inclusion of longer periods (up to 10 s) caused the results to become more variable, a fact that we attribute to the general inadequacies of the short-period instrumental response at longer periods. The splitting analysis in the region of the large transverse amplitudes (at a station about −15 km distance along the profile) is shown in Figure 4 for a period range between 2 and 5 s (note the scaling of the error bars as explained in the Figure 4 caption). Horizontal waveform components and particle motions are shown before and after application of an inverse splitting operator that best minimizes the energy of the transverse component. The transverse energy is removed successfully and the particle motion is linearized parallel to the theoretical back azimuth of the event (61°). The splitting analysis at shorter periods requires some further considerations due to the occurrence of an additional minimum of the transverse component energy as function of the two splitting parameters (separated by about 90° in Figure 4). However, this does not pose a problem in our analysis as the (apparent) splitting parameters are not interpreted directly in terms of anisotropic model properties. To resolve possible ambiguities at shorter periods, we consistently choose the parameter combination (the transverse energy minimum) that is closer to the (unique) minimum at longer periods (5–7 s). A more detailed discussion of this is given in the electronic supplements of *Rümpker et al.* [2003]. There it is also shown that the agreement between observations and modeling is not only limited to waveforms and splitting parameters but extents to the structural details of the transverse energy surface. This fact may be useful in future studies, where the comparison between observed and modeled waveforms could be based on the corresponding transverse energy surfaces, without the need to specify (possibly nonunique) splitting parameters. A direct comparison of waveforms, on the other hand, seems less promising due to complications related to the source characteristics.

[6] In the shorter periods range (2–5 s), the measurements of polarization directions of the fast shear wave (φ) vary between N5W and N15E along the profile (Figure 5). Consistently larger values of φ are found within the 40-km-wide zone, which coincides with larger transverse waveform components. The delay times are relatively uniform with values of about 1.5 s. At longer periods (5–7 s), the

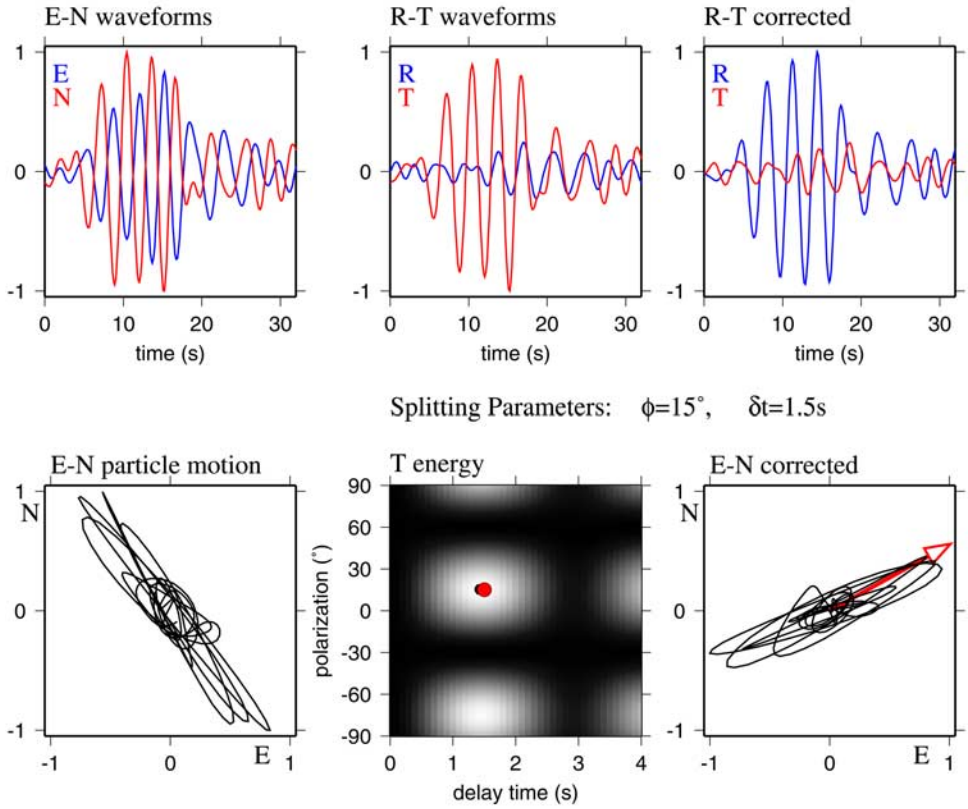

Figure 4. Shear wave splitting analysis for observed seismograms for a station at −15 km distance along the profile. Horizontal waveform components and particle motions are shown before and after application of an inverse splitting operator that minimizes the energy on the transverse component. The resulting splitting parameters are indicated by the solid red dot in the T component energy distribution. The red arrow (E-N corrected) points in the direction of the back azimuth for the event (61°). The splitting analysis is performed for periods of 2–5 s.

results at neighboring stations are slightly more variable due to their poorer signal-to-noise ratio. In the central region to the west of the Dead Sea transform fault delay times are consistently larger by 0.3 to 0.5 s, whereas the fast polarization direction is reduced by up to 15° relative to the short-period estimates.

3. Waveform Modeling and Inversion

[7] In order to explain the observed frequency-dependent lateral variations of splitting parameters along the profile a relatively complex model of elastic anisotropy in the crust and mantle beneath the profile is required. However, taking into account the overall structure of the Dead Sea transform system at the location of the profile [*DESERT Group*, 2004], we consider a two-dimensional Earth model to be appropriate and thus neglect any along-strike changes in Earth properties. Rather than deriving individual models of anisotropy for each single station followed by the compilation of a two-dimensional model, we perform a simultaneous inversion of the data of all stations and frequency bands by finite difference (FD) simulations of the wave field. In media with vertical and lateral variations of anisotropy, wave field diffraction may influence the determination of *SKS* splitting parameters [*Alsina and Snieder*, 1995; *Rümpker and Ryberg*, 2000]. In such cases the direct interpretation of splitting parameters in terms of medium properties becomes difficult. This is avoided here by the comparison with FD modeling.

[8] In our models, variations of anisotropy are accounted for by two-dimensional anisotropic block structures. In addition to its geometrical parameters (widths and positions in crust and mantle), every block is characterized by the magnitude of anisotropy and the orientation of the symmetry axis (Figure 6). The magnitude of the anisotropy is determined from the relative velocity difference between the vertically propagating shear waves. Also, in view of the transformational tectonic regime considered here and to limit the variability of the models, we assume orthorhombic symmetry with a horizontally aligned symmetry axis. The effective isotropic shear wave velocities are 3.5 km/s for the crust and 4.5 km/s for the mantle, respectively. In our modeling, the principal structure beneath the profile is characterized by an anisotropic crust extending to a depth of 35 km [*DESERT Group*, 2004] and a 100-km-thick anisotropic mantle layer directly beneath it. This choice for thickness of the mantle layer is based on estimates for the strength of anisotropy in the mantle [*Savage*, 1999]. A further separation into lithosphere and asthenosphere (as, e.g., *Hofstetter and Bock* [2004]) is not considered here due to the general inadequacy of *SKS* phases to resolve anisotropic depth variations in detail and due to

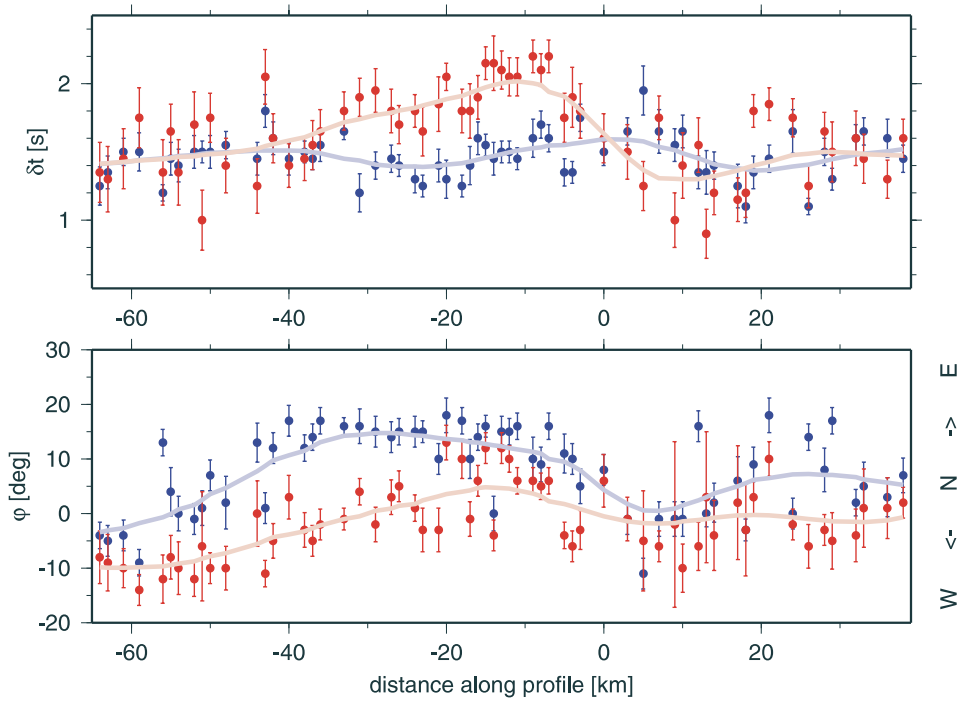

Figure 5. (bottom) Fast axis direction φ and (top) delay time δt along the profile (a distance 0 km corresponds to the surface location of the Dead Sea transform fault, station 54). Dots indicate the individual measurements, red colors correspond to the period band 5–7 s, and blue colors are the results for the period band 2–5 s The error bars have been derived from the 95% confidence region and have been scaled by a factor of 0.4 for presentation purposes. The lines are the result of spatial smoothing within a sliding window.

the limited azimuthal coverage. In view of lateral variations of splitting parameters along the profile (Figure 5), we limit the number of anisotropic domains (blocks) within the crust (respectively mantle) to 3, such that the most complex models considered here consist of up to six distinct anisotropic blocks. Depending on the observations, other model parameterizations might be more appropriate, that is, a smooth but laterally variable distribution of anisotropic properties could be described by splines, and a priori known geometrical information (e.g., crustal thickness, subduction geometry etc.) could also be considered. Given the tectonic regime at the Dead Sea transform system we would expect rather abrupt changes of the anisotropic properties, hence we think that simple block structures are justified.

[9] The principal steps in the inversion procedure are as follows: (1) An anisotropic model of the crust and mantle beneath the profile is constructed according to the schematic model given in Figure 6. (2) The two-dimensional model of the Dead Sea transform system is projected and rotated onto a near-vertical plane that is defined by the slowness of the incoming wave front. (3) *SKS* waveforms are calculated using a two-dimensional FD formulation of the complete inhomogeneous anisotropic wave equation. (4) The frequency-dependent splitting analysis is applied to the calculated waveforms. (5) The misfit between the (smoothed) splitting parameters from observed and calculated waveforms is determined from the cumulative misfit (RMS) of the delay times and fast axes for all stations in both period bands.

[10] The goal is to find models that minimize the misfit by changing the geometrical and anisotropic properties of the two-dimensional block structures. Each model is defined by up to four geometrical parameters, i.e., horizontal positions of the left and right boundaries of the two central

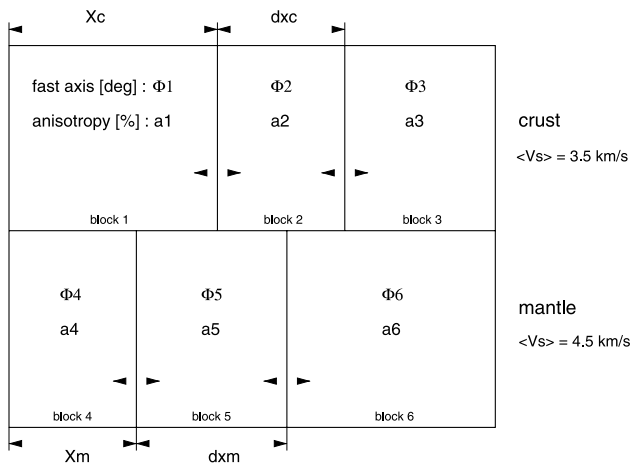

Figure 6. Block model used for the inversion. Each block is characterized by homogeneous anisotropy. Free parameters are block position and width (X_c, dX_c, and X_m dX_m) horizontal symmetry axis direction (Φ in degrees), and magnitude of anisotropy (a in percent). The model is subdivided into an anisotropic crust (35 km thick) and upper mantle anisotropic layer (100 km thick).

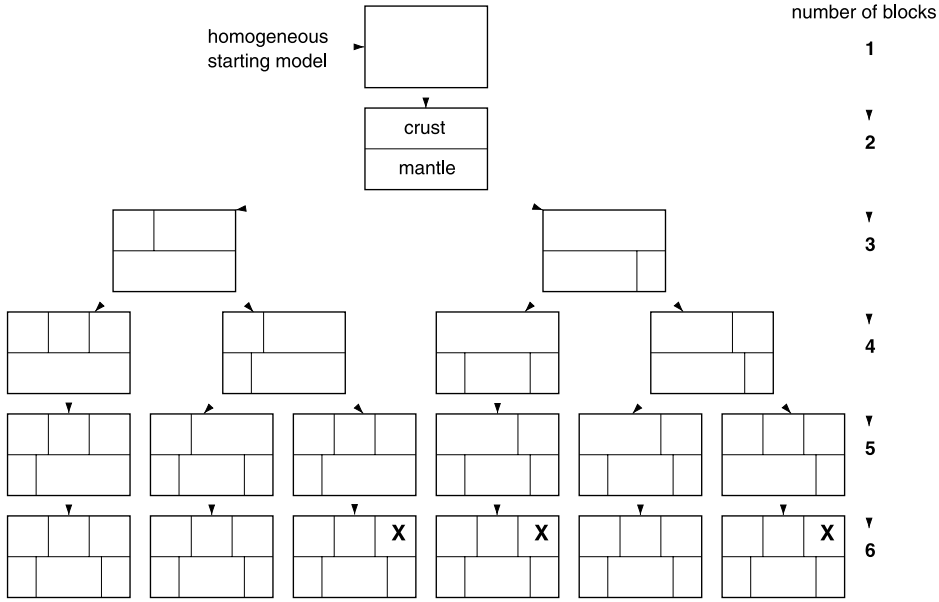

Figure 7. Inversion results using a local search algorithm (downhill simplex). The initial starting model exhibits homogeneous anisotropy in the crust and mantle. To improve the fit between predicted and observed splitting parameters, additional layers or blocks with distinct anisotropic properties are subsequently introduced. Models and predicted distribution of splitting parameters for models marked with X are shown in Figure 9.

blocks in the crust and mantle, and by 12 anisotropic constants, i.e., the magnitude of the anisotropy and direction of the subhorizontal symmetry axis within each block. The calculation of the misfit requires time-consuming finite difference modeling and a grid search over possible splitting parameters for all stations. A ''complete'' grid search over all 16 model parameters is not practically feasible. We therefore apply two different strategies to scan the parameter space for suitable models. The first involves a downhill simplex algorithm, where suitable parameters are found by systematic variations starting from an initial model. A second, more global approach, employs a genetic algorithm and allows for larger variations of the model parameters. This search gives additional information about the resolution of individual model parameters.

3.1. Local Parameter Search: Simplex Method

[11] In downhill simplex algorithm (DS) [*Nelder and Mead*, 1965; *Press et al.*, 1992] the simplex, a geometrical figure consisting, in N dimensions, of N + 1 points, is moved downhill on the topography of the objective function by a series of modifications (''reflection'', ''expansion'' or ''contraction'' of the simplex), until a minimum is found. DS is regarded as a moderately fast and robust local search algorithm well suited when the misfit function is well behaved and smooth. It can efficiently follow long flat valleys, and squeeze through saddle points, and has therefore pseudoglobal capabilities [*Charbonneau*, 2002]. However, in cases of misfit functions with many, not well-defined, local minima it may fail to converge to the global minimum. The solution is dependent on choice of starting model and the choice of ''distances'' between the starting simplex points.

[12] Taking this into account, we search for optimal parameters by successively increasing the complexity of anisotropic variations within the model. Therefore the initial starting model consists of a single, homogeneous anisotropic layer without any distinction between anisotropic domains of the crust and mantle. During further steps the number of anisotropic blocks is systematically increased (up to 6, see Figure 7) to achieve a better fit to the observed splitting parameters.

[13] Application of the simplex method to the single-layer model leads to values of 4.7% and 4° for the strength of the anisotropy and the symmetry axis orientation, respectively. In this case, these values can be related directly to the observed splitting parameters and they approximately represent the averages of the observed fast polarization directions and delay times. We then allow for vertical variations of anisotropy and distinct anisotropic domains in the crust and mantle by introducing a second anisotropic block. Using the anisotropic parameters of the previously derived model as starting values, a new simplex search leads to a model with slightly stronger anisotropy in the crust (6%) than in the mantle (4%). While this model can account for the observed frequency dependence to some degree, it still lacks any lateral variations. This can be overcome by introducing a third anisotropic block into either the crust or the mantle. The third block is added into the crust or mantle by placing its initial boundary at the center of the model range before the simplex search is started for all parameters. The two resulting models explain the observation better; that is, the RMS misfit is decreased. By taking the last optimized model and systematically introducing additional blocks (higher model complexity) we construct a set of models (see tree structure in Figure 7) that explain the observed shear wave splitting with an increased accuracy. This stepwise approach is based on finding improved models by adding three new parameters (dimensions), i.e., one geometrical

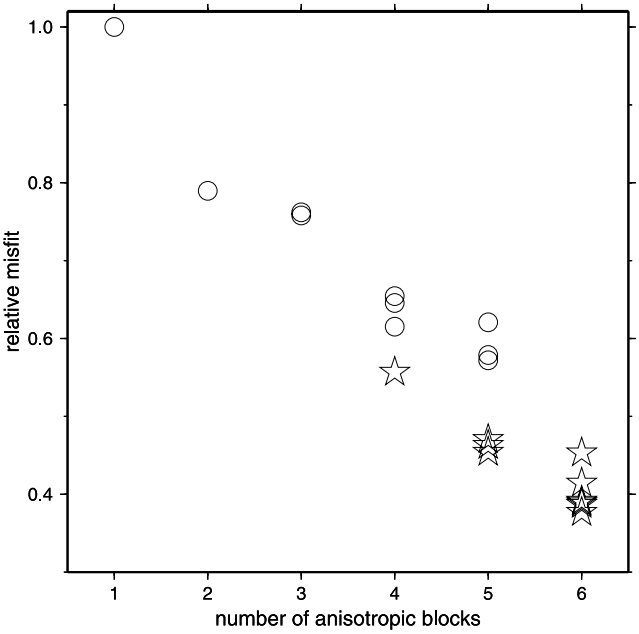

Figure 8. Reduction of the misfit (synthetic versus observed splitting parameters) of the best fitting models obtained from the simplex search (Figure 7) as function of the number of anisotropic blocks in the model. The misfit is normalized to the best fitting one-block model. Stars present models consisting of three mantle blocks; other models tested are indicated by circles. Note that all models with three mantle blocks exhibit a significantly reduced misfit within their class, indicating the significance of anisotropic inhomogeneities in the mantle.

and two anisotropic properties to the best fitting model of the previous step (see Figure 8). Models consisting of more than six blocks do not lead to a further significant reduction of the misfit. It is interesting to note that all models exhibiting three anisotropic blocks in the mantle are characterized by a significantly reduced misfit (Figure 8). This supports our previous interpretation of the observations in terms of a vertical decoupling zone in the mantle between the African and Arabian lithospheric plates [*Rümpker et al.*, 2003].

[14] Our approach leads to suite of block models that explains the observed shear wave splitting with increased accuracy. Given the character of this local search, neighboring models within the tree structure are only slightly different; that is, they are located close to each other in the model parameter space. The three best fitting six-block models ($\sigma < 0.4$, where σ is the relative misfit normalized to the misfit of the one-block model) exhibit remarkably similar characteristics (Figure 9). Further support for the validity of the best fitting model comes from the comparison between observed and calculated transverse/radial amplitude ratios as a function of frequency (Figure 3). While the local search approach leads to well-fitting models quickly and is computationally fast, it does not solve the question whether these models are unique and whether there might be a chance that completely different models might fit the observations even better. Global search algorithms help to answer this question.

3.2. Global Parameter Search: Genetic Algorithm

[15] To evaluate the possibility of models with distinctly different parameters of anisotropy that can also explain the observed shear wave splitting we carried out a more global search of model parameters based on a genetic algorithm (GA). GAs search a multimodal parameter space for (global) maxima by using mechanics of natural selection and natural genetics [*Holland*, 1975; *Goldberg*, 1989; *Carroll*, 1996]. They are very efficient global search methods capable of dealing with a large parameter space and misfit functions with many local minima. The parameters describing models are first coded into binary strings. A population of binary strings is modified by three operators, namely reproduction (selection), crossover and mutation. In the reproduction step individual strings are copied to the next generation according to their objective function values in a sense that higher values have higher probabilities to be copied. In the next step, offsprings are created from this mating pool by assembling substrings of parent binary strings. Finally, random mutations of single bits are performed on the population with a chosen (low) probability. This procedure is applied through many generations yielding a broad sampling of the parameter space while revealing one or more minima of the misfit function.

[16] In view of the results from the simplex approach, in the following we only consider six-block structures, which are determined by 16 model parameters. We use a geometrical discretization of $\sim$0.5 km for the geometrical parameters (location block boundaries) and limit the minimal block size to 15 km. The discretization of the material properties is 0.08% within the range of 0 and 10% for the magnitude of the anisotropy and $\sim 1.4^\circ$ within the range of -90° and 90° for the symmetry axis direction. We used a suite of 100 models within one generation.

[17] In our application of the algorithm we used the starting population in which the individuals emanated from the local (simplex) search [see, e.g., *Mathias et al.*, 1994] plus a number of additional random models. We used a population size of 100, mutation probability of 0.01, a (uniform) crossover probability of 0.5, and a creep mutation probability of 0.04. With these setting we intended to force the GA toward a broad sampling of the parameter space, while sacrificing some convergence speed.

[18] With an increasing number of model generations the data misfit decreases. The cumulative number of evaluated models exceeds 28,000, representatively scanning the entire model space. Figure 10 presents the result of the search. It shows the misfit of all evaluated models as eight two-dimensional cross sections of our 16-dimensional model space (see Figure 6). It can be seen in those projections that the model space was systematically scanned. With some exceptions, all projections show one main "cluster" of well-fitting models. The "width" of the main cluster can be used to constrain the resolution of the individual model parameters [*Haberland et al.*, 2003]. Judging visually from Figure 10, we estimated the resolution of the geometrical parameters to be around 5 km, the resolution of the fast axes to be between 5° and 10°. The resolution of the magnitude of the anisotropy is of the order of 1%. Of course, these

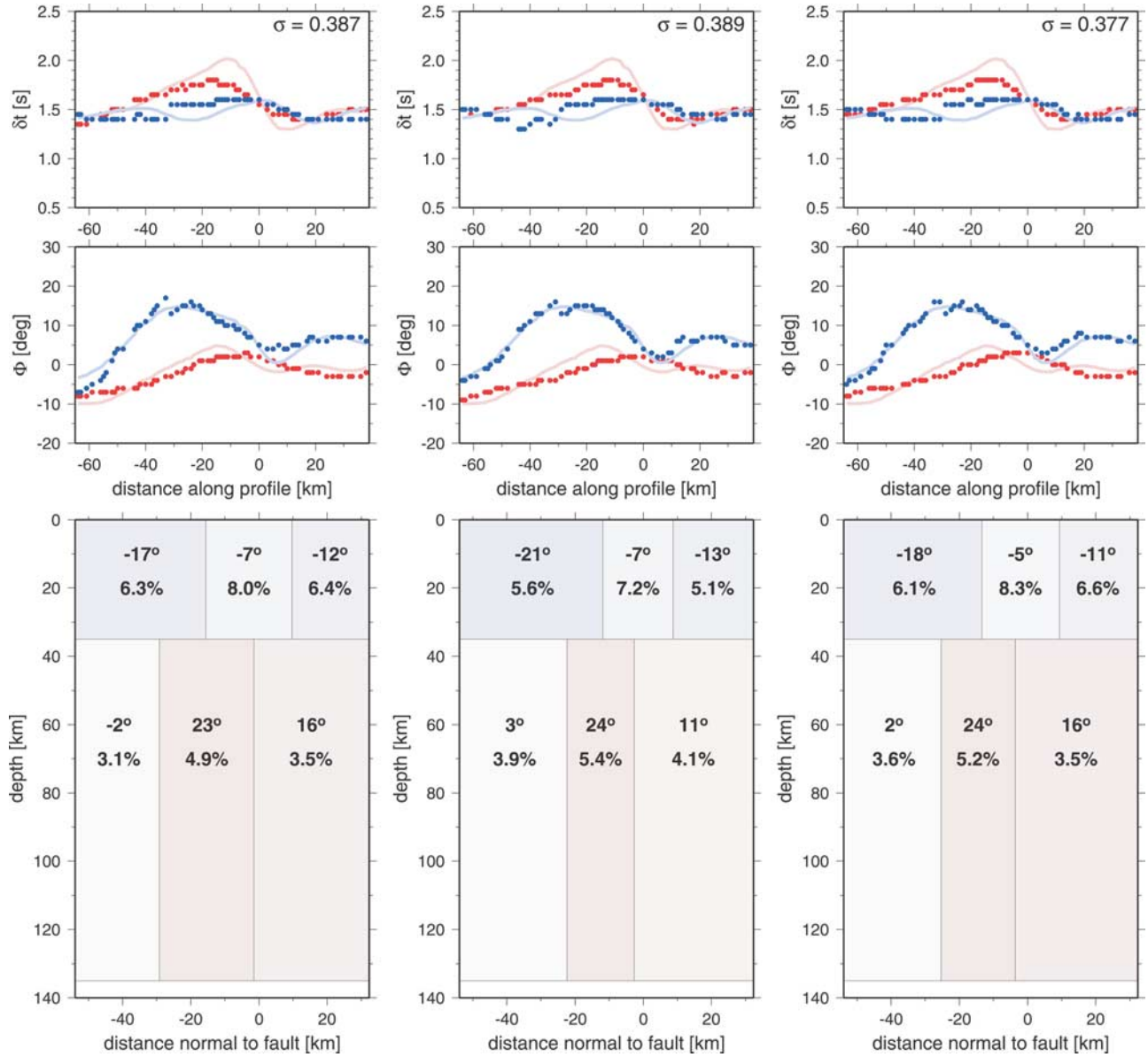

Figure 9. (bottom) Models and (top) predicted distribution of splitting parameters for the three best fitting models of the simplex search (marked with X in Figure 7). The orientation of the symmetry axis and the values of the magnitude of the anisotropy are given in each block (Figure 9, bottom). Additionally, the orientation of the symmetry axis is color coded. Red and blue symbols (top, delay time δt; middle, fast polarization direction φ) represent the predicted splitting parameters for both frequency bands analyzed; light red and light blue are the smoothed observed splitting parameters (as in Figure 5).

estimates do not take into account any trade-offs between the parameters, which can be expected, i.e. larger crustal anisotropy could be partially compensated by smaller mantle anisotropy and vice versa. All initial starting models, except for the random ones, belong to the main cluster. Interestingly, there are two additional groups of models at some distance from the main cluster that also satisfy the observed splitting parameters to some degree (see Figure 10, top left).

4. Cluster Analysis of Inversion Results

[19] To evaluate the possibility of coexisting groups or clusters of well-fitting models which are not closely spaced in model space, we performed a cluster analysis of the best fitting models. This subset has been selected from all models evaluated during the genetic algorithm search. The set of 2444 best fitting models was analyzed in order to sort solutions into groups of similar association by a hirarchical cluster analysis [*Swan and Sandilands*, 1995]. The main clusters were visualized in the first three dimensions of a principal component system.

[20] The cluster analysis requires the calculation of a distance between different models, the grouping of the models into a binary, hierarchical cluster tree by linking together those pairs that are in close proximity, and the division of the tree into clusters. All of the 16 model parameters in the data set were normalized to avoid scaling

Table 1. Size and Nonscaled Centroid Coordinates of the Three Largest Clusters[a]

	Cluster 1	Cluster 2	Cluster 3
Number of models	2373	20	19
X_c, km	−13.89	−38.86	−25.25
dX_c, km	22.74	18.31	34.18
X_m, km	−25.40	−27.34	−25.80
dX_m, km	21.39	16.46	26.02
Φ_1, deg	−17.15	−28.35	−16.30
a_1, %	6.03	5.08	7.60
Φ_2, deg	−5.03	−21.47	−7.80
a_2, %	8.34	4.51	6.85
Φ_3, deg	−11.65	−3.83	−15.26
a_3, %	6.78	6.57	5.83
Φ_4, deg	2.04	−1.56	10.18
a_4, %	3.48	3.85	2.91
Φ_5, deg	24.67	21.83	26.08
a_5, %	5.33	5.77	4.43
Φ_6, deg	16.08	12.19	13.32
a_6, %	3.52	3.70	4.14

[a] X_c and X_m are the positions of the second crustal and mantle blocks, dX_c and dX_m are their widths, and Φ_n and a_n are the symmetry axis and magnitude of anisotropy of the nth block; see Figure 6.

effects which may distort the proximity calculations (mean 0, standard deviation 1). The analysis was carried out with an Euclidean distance between different models and a linkage algorithm using the Euclidian distance between the centroids of two groups. The resulting correlation coefficient of 0.898 is statistically significant. A stable grouping was achieved by division of the binary cluster tree into increasing numbers (from 5 to 20) of clusters. Table 1 describes the three largest clusters of an 10 cluster subdivision and their centroid coordinates.

[21] In order to visualize the clusters an appropriate projection of all 16 parameters into a three-dimensional system was necessary. Here, the first three directions of a principal component analysis (PCA) of the data were selected. PCA has three effects [*Jolliffe*, 1986]: it orthogonalizes the components of the input vectors (so that they are uncorrelated with each other); it orders the resulting orthogonal components (principal components PCs) so that those with the largest variation come first; and it eliminates those components that contribute the least to the variation in the data set. Figure 11 shows the results of the PCA. More than one third of the data variance is determined by the three largest components. This result suggests that a visualization of the position of the clusters to each other can actually be performed in three dimensions (Figure 12).

[22] The analysis shows that there is one main cluster represented by the majority of the evaluated models. In addition we found two other clusters at some distance from the main cluster. Figure 13 shows the corresponding models with their splitting parameters. However, the smallest (normalized) misfit ($\sigma < 0.4$) is found for the model that represents the main cluster. The characteristics of this model are very similar to those previously obtained using the simplex approach (Figure 9).

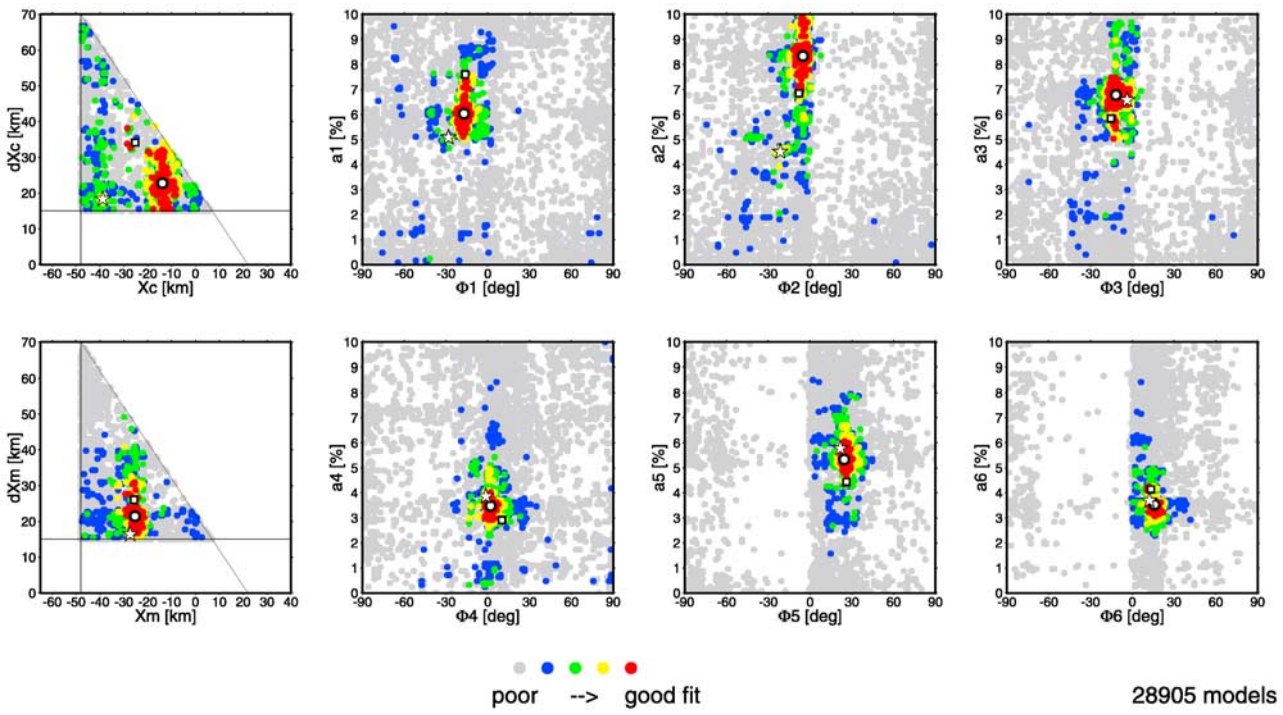

Figure 10. Two-dimensional representation of the model space. The diagrams show the color-coded misfits projected to the coordinate system of pairs of independent parameters (X_c/dX_c, X_m/dX_m, and Φ_n/a_n). Note the clustered character of well-fitting models (blue, green, yellow, and red dots). Red dots represent the highest degree of agreement between predicted and observed splitting parameters. The star, open circle, and square indicate the model values for the centers of the three main clusters determined by the cluster analysis (see Figures 12 and 13). The triangular shape of the diagrams on the left is caused by the fact that we required the block size to be larger than 15 km.

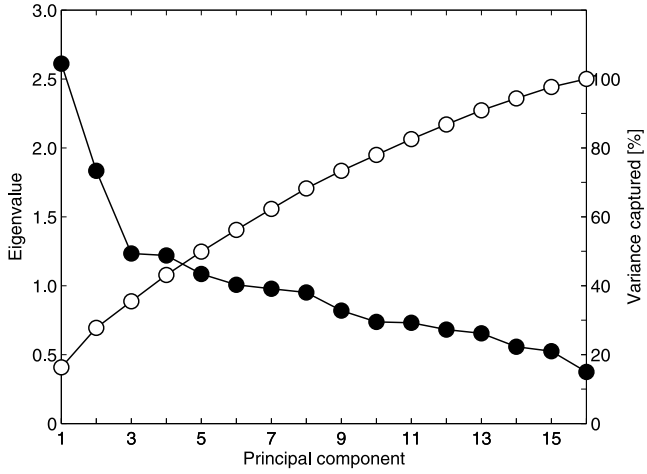

Figure 11. Eigenvalues (solid circle) and staged variances (open circles) of a principal component analysis of all fitting models. The first three principal components (orthogonal linear combinations of the 16 model parameter) capture more then one third of the total variance.

[23] These models not only predict the observed splitting parameters but also exhibit a frequency-dependent transverse/radial amplitude ratio similar to that deduced from the data (Figure 3), which further supports the validity of these three best fitting models.

5. Concluding Remarks

[24] In this study we have used frequency-dependent and spatially varying splitting parameters observed from *SKS* phases along a linear array to constrain the anisotropic properties in the crust and mantle beneath the Dead Sea transform fault. The combination of FD waveform modeling with two alternative inversion approaches leads to a consistent set of two-dimensional anisotropic block models. There is no inherent limitation to the orientation of the horizontal symmetry axes and the strength of the anisotropy within the anisotropic domains of the models. Fixed parameters are the thicknesses of the (anisotropic) crust and the anisotropic layer in the mantle. In our example the depth structure of the anisotropy beneath the profile is mainly constrained by variations of splitting parameters with frequency. With the simplex method we first determined a set of models which explain the observed distribution of splitting parameters. A significant reduction of the relative misfit between observed and modeled splitting parameters is obtained for models with three distinct anisotropic domains in the mantle. The three best fitting models ($\sigma < 0.4$) resulting from the simplex approach are characterized by average anisotropies in the crust and mantle of about 6% and 4%, respectively, whereas the symmetry axis orientation of the two layers (crust and mantle) is oblique by about 30°. The 20–25 km wide central region in the mantle exhibits increased anisotropy by more than 1.3% and a change in symmetry axis orientation by about 10° compared to the surrounding mantle. Similarly, the central block in the crust is also more highly anisotropic (by about 1–2%). The six-block structures derived from the simplex method have been used as a basis to perform a more global search for good fitting models using a genetic algorithm technique, which also provided error estimates for the anisotropic properties. The anisotropic properties of the best fitting model ($\sigma < 0.4$) obtained from the GA search are consistent with results from the more local simplex approach. We consider this similarity as strong evidence for the fact that the data cannot be sufficiently explained by a completely different set of anisotropic model parameters. These results support the interpretation of *Rümpker et al.* [2003], where the narrow highly anisotropic zone with fault-parallel symmetry axis in the mantle is thought to represent a vertical boundary layer between the Arabian and African plates.

[25] Given the tectonic setting of the study area (see Figure 1), we expect a predominantly two-dimensional anisotropic structure with horizontally oriented symmetry axes beneath the profile. However, we can not completely exclude the possible influence of three-dimensional isotropic inhomogeneities off the profile on the waveforms. It is straightforward to apply the data analysis and inversion techniques presented here to array data for multiple earthquakes. One may suspect that the inferred depth-dependent anisotropic structures could lead to characteristic variations of splitting parameters as function of back azimuth at a single station [*Silver and Savage*, 1994]. The largest variations are expected for stations above the central region, where differences of anisotropy in the crust and mantle are more pronounced. However, the small width of the decoupling zone and the asymmetry the anisotropic features with respect to back azimuth will likely obscure the characteristic pattern of splitting parameters expected for layered anisotropic structures.

[26] Instead of inverting for block models, other parameterizations, including more complex models using a smooth (i.e., interpolated) distribution of anisotropic properties, can be introduced. The incorporation of known geometrical constraints of crustal and upper mantle structures and the extension of our approach to three dimensions

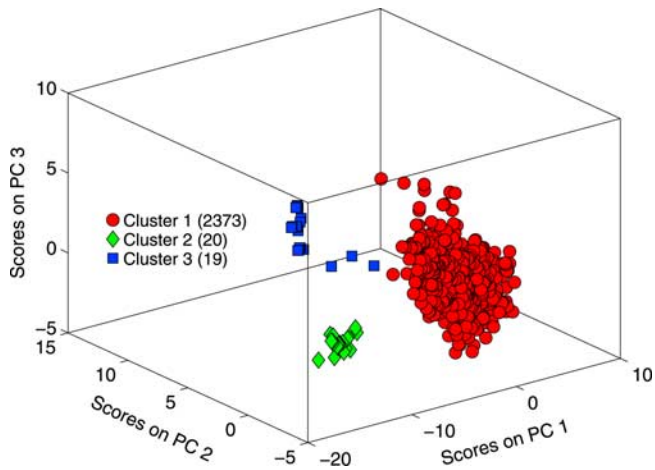

Figure 12. Visualization of the main clusters of all fitting models in the system of the three largest principal components (PC1, PC2, PC3). Note the clear separation of the clusters corresponding to different models. The separation of the clusters can also be seen in Figure 10.

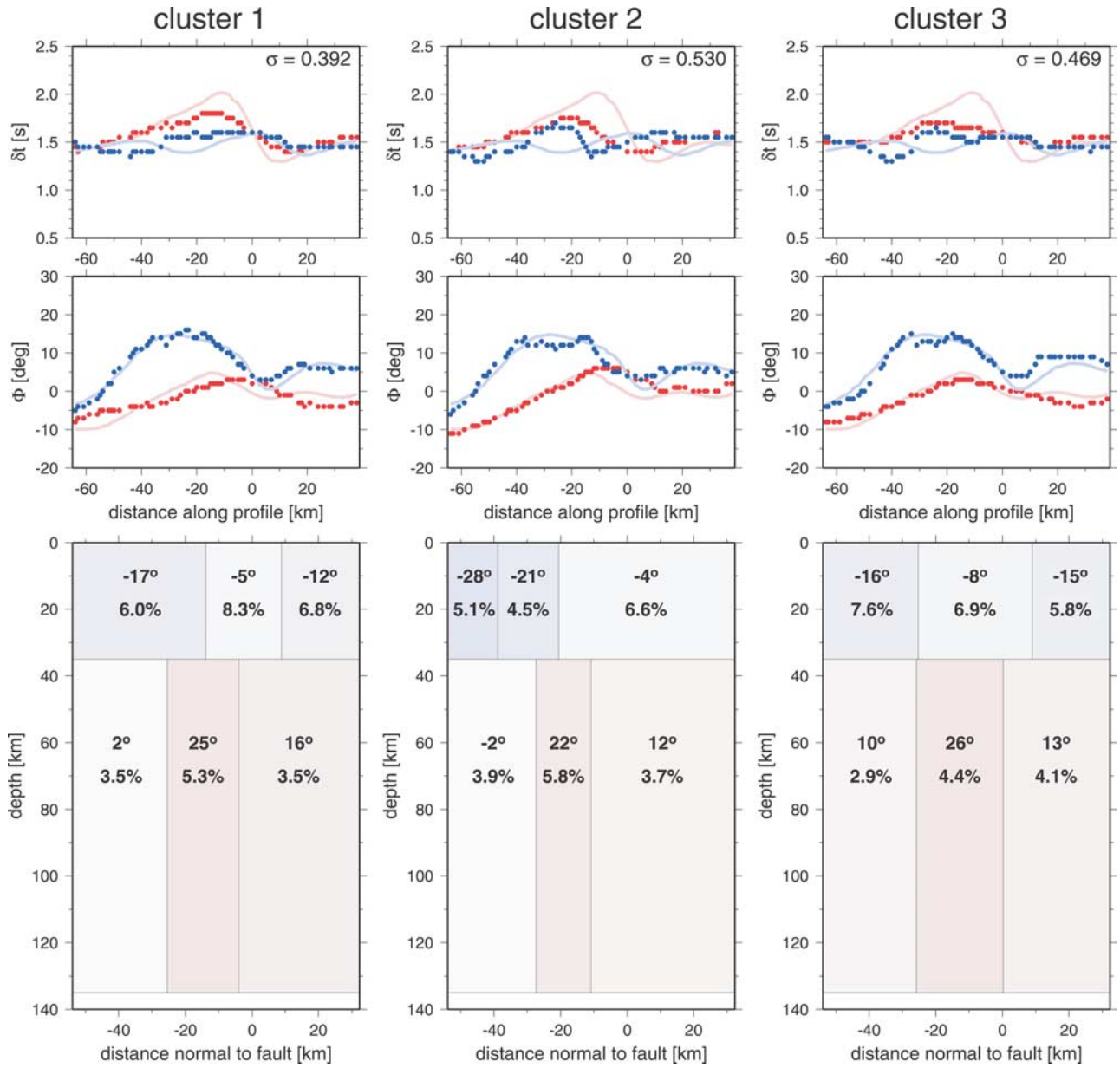

Figure 13. (bottom) Models and (top) predicted distribution of splitting parameters for the centers of the three clusters (red, blue, and green) given in Table 1 and Figure 12. The orientation of the symmetry axis and the values of the magnitude of the anisotropy are given in each block (bottom diagrams). Additionally the orientation of the symmetry axis is color coded. All models (bottom) are characterized by a central mantle zone of increased anisotropy, which is differently oriented with respect to its neighbor. Red and blue symbols (top, delay time δt; middle, fast polarization direction φ) represent the predicted splitting parameters for both frequency bands analyzed; light red and light blue are the smoothed observed splitting parameters (as in Figure 5).

could be appropriate for two-dimensional seismological array design.

Appendix A: Dominant Transverse Displacement Components

[27] Dominant transverse versus radial displacement components can occur even in simple one-layer anisotropic structures. The effect can be explained by considering the frequency domain expressions for the radial and transverse displacement components due to a single anisotropic layer [*Rümpker and Silver*, 1998]

$$u_r = \cos(\omega\delta t/2) - i\sin(\omega\delta t/2)\,\cos[2(\varphi - \varphi_i)], \tag{A1}$$

$$u_t = -i\sin(\omega\delta t/2)\,\sin[2(\varphi - \varphi_i)] \tag{A2}$$

with splitting parameters δt and φ, initial polarization φ_i, and frequency ω. Assuming a plane harmonic wave of

period T, the radial component u_r vanishes under the conditions that

$$\delta t = T/2, \tag{A3}$$

$$|\varphi - \varphi_i| = \pi/4. \tag{A4}$$

For our observations, with a dominant period $T = 3.2$ s and a back azimuth $\varphi_i = 61°$, this corresponds to splitting parameters $\varphi = 16°$ and $\delta t = 1.6$ s. Such values are obtained in our splitting analysis at stations that exhibit the largest transverse amplitudes for periods between 2 and 5 s (see, e.g., Figure 2). Whenever the above conditions are met approximately, a dominant transverse component arises, even for the single anisotropic layer. A further prerequisite is a waveform of approximate sinusoidal shape (harmonic wave), whereas a simple pulse shape (δ function) does not result in a vanishing radial component. In our case, the effect became apparent due to the short-period instruments used in the experiment and the application of a band-pass filter for periods between 2 and 5 s resulted in its amplification. At longer periods, between 5 and 7 s, the amplitudes of the transverse components are more similar to those of the radial components. This is in agreement with the long-period limit, in which case the radial component is expected to dominate.

[28] **Acknowledgments.** The authors would like to thank the Deutsche Forschungsgemeinschaft for supporting this project. Seismic sensors and recorders for the field experiment were provided by the Geophysical Instrument Pool Potsdam (GIPP) of GeoForschungsZentrum Potsdam. We thank James Wookey, an anonymous reviewer and Frederik Simons (AE) for helpful comments.

References

Alsina, D., and R. Snieder (1995), Small-scale sublithopsheric continental mantle deformation: Constraints from *SKS* splitting observations, *Geophys. J. Int.*, *123*, 431–448.

Blackman, D. K., J.-M. Kendall, P. R. Dawson, H.-R. Wenk, D. Boyce, and J. Phipps Morgan (1996), Teleseismic imaging of subaxial flow at mid-ocean ridges: Travel-time effects of anisotropic mineral texture in the mantle, *Geophys. J. Int.*, *127*, 415–426.

Bock, G., R. Kind, A. Rudloff, and G. Asch (1998), Shear wave anisotropy in the upper mantle beneath the Nazca plate in northern Chile, *J. Geophys. Res.*, *103*, 24,333–24,345.

Brechner, S., K. Klinge, F. Krüger, and T. Plenefisch (1998), Backazimuthal variations of splitting parameters of teleseismic *SKS*-phases observed at the broadband stations in Germany, *Pure Appl. Geophys.*, *151*, 305–331.

Carroll, D. L. (1996), Chemical laser modeling with genetic algorithm, *Am. Inst. Aeron. Astron. J.*, *34*(2), 338–346.

Charbonneau, P. (2002), An introduction to genetic algorithms for numerical optimization, *NCAR Tech. Note NCAR/TN-450+IA*, High Altitude Obs., Natl. Cent. for Atmos. Res., Boulder, Colo.

DESERT Group (2004), The crustal structure of the Dead Sea Transform, *Geophys. J. Int.*, *156*, doi:10.1111/j.1365–246X.2004.02,143.x.

Fischer, K. M., E. M. Parmentier, A. R. Stine, and E. R. Wolf (2000), Modeling anisotropy and plate-driven flow in the Tonga subduction zone back arc, *J. Geophys. Res.*, *105*, 16,181–16,191.

Fouch, M. J., K. M. Fischer, E. M. Parmentier, M. E. Wysession, and T. J. Clarke (2000), Shear-wave splitting, continental keels, and patterns of mantle flow, *J. Geophys. Res.*, *105*, 6255–6275.

Goldberg, D. E. (1989), *Genetic Algorithms in Search, Optimization, and Machine Learning*, Addison-Wesley, Boston, Mass.

Haberland, C., A. Agnon, R. El-Kelani, N. Maercklin, I. Qabbani, G. Rümpker, T. Ryberg, F. Scherbaum, and M. Weber (2003), Modeling of seismic guided waves at the Dead Sea transform, *J. Geophys. Res.*, *108*(B7), 2342, doi:10.1029/2002JB002309.

Hall, C. E., K. M. Fischer, E. M. Parmentier, and D. K. Blackman (2000), The influence of plate motion on three dimensional back arc mantle flow and shear wave splitting, *J. Geophys. Res.*, *105*, 28,009–28,033.

Hartog, R., and S. Y. Schwartz (2000), Subduction-induced strain in the upper mantle east of the Mendocino triple junction, California, *J. Geophys. Res.*, *105*, 7909–7930.

Hartog, R., and S. Y. Schwartz (2001), Depth-dependent mantle anisotropy below the San Andreas Fault system: Apparent splitting parameters and waveforms, *J. Geophys. Res.*, *106*, 4155–4167.

Hofstetter, R., and G. Bock (2004), Shear-wave velocity structure of the Sinai subplate from receiver function analysis, *Geophys. J. Int.*, *158*(1), 67–84.

Holland, J. (1975), *Adaption in Natural and Artificial Systems*, Univ. of Mich. Press, Ann Arbor.

Huang, W. C., F. J. Ni, F. Tilmann, D. Nelson, J. Guo, W. Zhao, J. Mechie, R. Kind, J. Saul, R. Rapine, and T. H. Hearn (2000), Seismic polarization anisotropy beneath the central Tibetan Plateau, *J. Geophys. Res.*, *105*, 27,979–27,989.

Jolliffe, I. T. (1986), *Principal Component Analysis*, Springer, New York.

Marson-Pidgeon, K., and M. K. Savage (1997), Frequency-dependent anisotropy in Wellington, New Zealand, *Geophys. Res. Lett.*, *24*, 3297–3300.

Mathias, K., D. Whitley, C. Stork, and T. Kusuma (1994), Staged hybrid genetic algorithm search for seismic data imaging, in *Proceedings of the IEEE Conference on Evolutionary Computation*, vol. 1, pp. 356–361, Inst. of Electr. Eng., New York.

Nelder, J., and R. Mead (1965), A simplex method for function minimization, *Comput. J.*, *7*, 308–313.

Polet, J., and H. Kanamori (2002), Anisotropy beneath California: Shear wave splitting measurements using a dense broadband array, *Geophys. J. Int.*, *149*, 313–327.

Polet, J., P. G. Silver, S. Beck, T. Wallace, G. Zandt, S. Ruppert, R. Kind, and A. Rudloff (2000), Shear wave anisotropy beneath the Andes from the BANJO, SEDA, and PISCO experiments, *J. Geophys. Res.*, *105*, 6287–6304.

Press, W. H., S. A. Teukolsky, W. T. Vetterling, and B. P. Flannery (1992), *Numerical Recipes in FORTRAN—The Art of Scientific Computing*, Cambridge Univ. Press, New York.

Rümpker, G., and T. Ryberg (2000), New "Fresnel-zone" estimates for shear-wave splitting observations from finite-difference modeling, *Geophys. Res. Lett.*, *27*, 2005–2008.

Rümpker, G., and P. G. Silver (1998), Apparent shear-wave splitting parameters in the presence of vertically-varying anisotropy, *Geophys. J. Int.*, *135*, 790–800.

Rümpker, G., T. Ryberg, G. Bock, and DESERT Seismology Group (2003), Boundary-layer mantle flow under the Dead Sea transform fault inferred from seismic anisotropy, *Nature*, *425*, 497–501.

Russo, R. M., and P. G. Silver (1994), Trench-parallel flow beneath the Nazca plate from seismic anisotropy, *Science*, *263*, 1105–1111.

Savage, M. K. (1999), Seismic anisotropy and mantle deformation: What have we learned from shear wave splitting, *Rev. Geophys.*, *37*, 65–106.

Silver, P. G., and M. K. Savage (1994), The interpretation of shear-wave splitting parameters in the presence of two anisotropic layers, *Geophys. J. Int.*, *119*, 949–963.

Swan, A. R. H., and M. Sandilands (1995), *Introduction to Geological Data Analysis*, Blackwell Sci., Malden, Mass.

Walker, K. T., G. H. R. Bokelmann, S. L. Klemperer, E. Gashawbeza, and A. Nyblade (2005), Shear-wave splitting around hot spots: evidence for upwelling related mantle flow, *Geophys. J. Int.*, in press.

C. Haberland, T. Ryberg, D. Stromeyer, and M. Weber, GeoForschungsZentrum Potsdam, Telegrafenberg, D-14473 Potsdam, Germany. (trond@gfz-potsdam.de)

G. Rümpker, Fachbereich Geowissenschaften/Geographie, J. W. Goethe-Universität Frankfurt, D-60323 Frankfurt am Main, Germany.